Nanoscale

PAPER

View Article Online
View Journal | View Issue

Cite this: *Nanoscale*, 2025, **17**, 17846

2 eV band gap tuning and optical properties of $AgIn_5S_8$ quantum dots†

Biljana Pejova,*[a] Julio A. do Nascimento,[b] Fayzah Talbi,[b,c] Thomas Jack Fawcett-Houghton,[b] Adam Kerrigan,[b,e] Leonardo Lari,[b,e] Richard E. Douthwaite,[d] Ljupcho Pejov[a] and Vlado K. Lazarov*[b,e]

In this work, we demonstrate the colloidal bottom-up synthesis of spinel $AgIn_5S_8$ quantum dots (QDs) with tunable optical properties. The QD size, and consequently their band gap energy (E_g), is effectively controlled by reaction temperature and ultrasound (US) irradiation. Under combined conditions of 75 °C and US irradiation, ultrasmall QDs with an average size of 2.6 nm are obtained, exhibiting a wide band gap of 3.77 eV. In the absence of US, reactions conducted at 55 °C and 75 °C yield larger QDs (~5 nm and 31 nm, respectively), with reduced band gaps of 3.09 eV and 2.18 eV. The elevated temperature (75 °C) suppresses sulfur-chain formation that otherwise limits growth at 55 °C, while acoustic cavitation induced by US enables narrowest size distribution. Annealing of as prepared QDs, at 200 °C for 2 h, promotes coalescence resulting in QDs with increased size of ~34 nm, with a bulk like band gap of 1.73 eV for QDs prepared without US. In contrast, annealing of the QDs, prepared with US, results in polycrystalline QDs with average size of ~21 nm. High-resolution transmission electron microscopy reveals a strong correlation between QD size, structural ordering and optical behavior. The as-prepared 2.6 nm QDs exhibit lower Urbach energy, attributed to their single-crystalline nature, unlike the less ordered QDs synthesized without US. Annealing improves structural ordering and reduces Urbach energy in QDs prepared at 75 °C, while stacking faults and grain boundaries in other QDs hinder such improvements. Photoluminescence measurements further confirm a strong relationship between QD structure, size, and emission characteristics. The synthesized $AgIn_5S_8$ QDs exhibit remarkable band gap tunability of up to 2 eV across the visible spectrum and sharp band-edge emission, underscoring their potential for applications in optoelectronic and biomedical devices. This work provides a robust and sustainable pathway to high-performance, non-toxic QDs, addressing a key bottleneck for their use in biocompatible and consumer electronics.

Received 24th April 2025,
Accepted 9th July 2025

DOI: 10.1039/d5nr01665g

rsc.li/nanoscale

1. Introduction

Colloidal quantum dots (QDs) have been extensively studied over the past few decades due to their tunable optical properties and compatibility with a broad range of applications. Synthesized *via* cost-effective and scalable colloidal methods, QDs can be readily integrated with diverse technological platforms such as silicon and flexible electronics, fiber optics, and textiles. In addition to their technological relevance, colloidal QDs serve as model systems for exploring fundamental processes in nucleation, crystal growth and surface chemistry.[1–5]

The quantum confinement effect allows the band gap of QDs to be precisely tuned by controlling their size and composition.[6–9] Their strong luminescence, narrow emission bandwidth and excellent photostability, combined with low toxicity in selected systems, make them promising candidates also for bioimaging, biosensing and diagnostic applications.[10–12] Particularly, ultrasmall QDs (<3 nm) are of great interest for biomedical use due to their ability to cross biological barriers and avoid immune recognition, mimicking the behavior of small-molecule drugs.[13,14]

To date, most QD research has focused on binary systems such as II–VI, III–V and IV–VI semiconductors.[15–19] However, these materials often incorporate toxic heavy metals (*e.g.* Cd, Pb, Hg), posing challenges for environmental and biomedical applications. This has motivated a shift towards less toxic alternatives such as ternary I–III–VI semiconductors (I = Cu, Ag; III = In, Ga,

[a]*Institute of Chemistry, Faculty of Natural Sciences and Mathematics, SS. Cyril and Methodius University, POB 162, 1000 Skopje, North Macedonia. E-mail: biljana@pmf.ukim.mk*
[b]*School of Physics Engineering and Technology, University of York, York, YO10 5DD, UK. E-mail: vlado.lazarov@york.ac.uk*
[c]*Department of Physical Sciences, Faculty of Science, University of Jeddah, P.O. Box 13151, Jeddah, 21493, Saudi Arabia*
[d]*Department of Chemistry, University of York, York, YO10 5DD, UK*
[e]*The York-JEOL Nanocentre, University of York, York, YO10 5DD, UK*
† Electronic supplementary information (ESI) available. See DOI: https://doi.org/10.1039/d5nr01665g

Al; VI = S, Se, Te).[20–26] These chalcogenide semiconductors, known for their broad structural and compositional tunability, offer direct band gaps in the visible range and high absorption coefficients (10^4–10^5 cm^{-1}).[12] Their properties can be further engineered through doping and phase control.

Among these, Ag–In–S based QDs are particularly attractive due to their versatile photoluminescence (PL) characteristics. Compared to other I–III–VI systems, $AgInS_2$ QDs exhibit smaller band gaps due to the influence of In^{3+} and S^{2-}, resulting in red to near-infrared emission.[27] Doping with smaller cations (*e.g.*, Ga^{3+}, Al^{3+}, Bi^{3+}, Zn^{2+}) can shift the PL toward shorter wavelengths (green or blue), offering tunable emission across the visible spectrum.[28–30] As such, Ag–In–S QDs are emerging as a non-toxic alternative for applications including biocompatible imaging, photocatalytic pollutant degradation and solar hydrogen production.[31–62] However, most studies to date have focused on $AgInS_2$, with limited work on other stoichiometries such as the spinel-phase $AgIn_5S_8$.

In this work, we focus on $AgIn_5S_8$, a direct-band-gap semiconductor with high PL quantum yield, energy convergence in the excited state, desirable for quantum light-emitting diode applications.[27,49,50] We demonstrate a low-temperature, aqueous-phase colloidal synthesis method – both with and without ultrasound assistance – for the preparation of $AgIn_5S_8$ QDs with controlled size and optical properties.

Unlike traditional syntheses in organic solvents which often require complex procedures and post-synthetic modifications (*e.g.* ligand exchange, silica coating) to achieve water dispersibility,[53] our aqueous-based approach directly yields water-dispersible QDs under mild conditions. Organic-solvent-based routes also tend to suffer from poor reproducibility and challenging scale-up. Importantly, aqueous synthesis of phase-pure $AgIn_5S_8$ QDs has been hindered by competing formation of secondary phases such as $AgInS_2$, In_2S_3, and Ag_2S.[54,55] Our method circumvents these limitations, producing phase-pure spinel $AgIn_5S_8$ QDs with exceptional band gap tunability.

We report the broadest band gap tuning range for any Ag-based ternary QD system to date, from 1.70 to 3.77 eV. By comparison, $AgInS_2$ QDs typically exhibit tunability only between 2.3 and 3.1 eV.[56] Moreover, previous attempts to achieve narrow, band-edge photoluminescence in I–III–VI QDs have been limited. Time-resolved PL and X-ray studies have indicated that broad emission in these systems originates from multiple donor–acceptor recombination pathways resulting in PL full width at half maxima (FWHM) exceeding 100–300 meV.[57–59] In contrast, our $AgIn_5S_8$ QDs exhibit significantly narrower PL linewidths: FWHM as low as ~25 meV in annealed samples and ~100 meV in as-deposited nanocrystals. These values are within or even better than industrial standards and notably better to those of typical II–VI QDs such as CdSe, CdTe and InP.[63,64]

Overall, this work advances the field by providing a green, scalable and reproducible synthesis of high-performance spinel Ag-based QDs, aligning with sustainable chemistry goals through low-energy processing and use of water as a safe solvent.

2. Experimental section

2.1. Synthesis of $AgIn_5S_8$ QDs with and without ultrasound

$AgIn_5S_8$ QDs were prepared using a bottom-up approach at 55 °C (QD-55) and 75 °C (QD-75), and at 75 °C with ultrasound (US) (QD-75US).

The main components of the reaction system are ionic precursors and a ligand agent. $AgNO_3$ and $In_2(SO_4)_3$ were used as cation (Ag^+ and In^{3+}) precursors, while thioacetamide, $(CH_3)CS(NH_2)$ is the sulfide precursor. Sodium thiosulfate, $Na_2S_2O_3$ was included in the reaction system as a ligand agent to control the concentrations of the relevant ions. This approach requires carefully controlled equilibria during the reaction process in the aqueous solution which are mutually and pH dependent, see ESI-1† for more details.

Synthesis of $AgIn_5S_8$ was achieved in all three approaches. We note that our aqueous medium method of $AgIn_5S_8$ QDs synthesis is greener compared to more severe organic-based synthesis. Furthermore, multi-bubble sonoluminescence (MBSL) conditions, in case of US-assisted route, are also quite mild[65] in comparison with the other typically high temperature wet chemical methods.

Synthesis of $AgIn_5S_8$ (QD-55) and (QD-75). The initial composition of the used reaction system was: 0.04 mol L^{-1} In^{3+}, 0.01 mol L^{-1} Ag^+, 0.3 mol L^{-1} $S_2O_3^{2-}$ and 0.3 mol L^{-1} $(CH_3)CS(NH_2)$. The solution was heated from room temperature to either 55 °C or 75 °C over a period of 15 min and maintained at 55 °C or 75 °C for a further 90 min before allowing to cool to room temperature. The synthesized samples were separated using filtration, washed with double deionized water and dried at room temperature.

Synthesis of $AgIn_5S_8$ (QD-75US). The prepared solution, with the same initial composition used for synthesis of QD-55 and QD-75 was heated from room temperature to 75 °C over a period of 10 min and maintained at 75 °C for 45 min before allowing to cool to room temperature. During heating the reaction system was sonicated by immersion of a high-intensity ultrasound horn using a home-made setup.[66–68] The frequency and the intensity of sinusoidal-like generated ultrasound irradiation were 20 kHz and 100 W cm^{-2}, respectively. After cooling the reaction system to room temperature, the obtained samples were filtrated, washed with double deionized water and dried at room temperature.

Of note during synthesis color changes were observed for all reactions. For QD-75US the reaction system went from transparent through greenish, yellow and orange to red (ESI Fig. 1†) with sonoluminescence[65,69,70] observed during the reaction and a redshift of the emitted colors suggesting QD growth during synthesis. The formed QDs absorb energy, released by acoustic cavitation and emit bright colors depending on their size-dependent energy spectrum. Similarly, for QD-55 and QD-75, chemiluminescence phenomenon is observed, with redshift of color change again indicating growth of QDs during the reaction process.

2.2. Characterization methods

Structural and optical properties of the synthesized QDs were investigated using powder X-ray diffraction (XRD), Scanning

Electron Microscopy (SEM), Transmission Electron Microscopy (TEM), Scanning TEM (STEM) and photoluminescence (PL).

XRD patterns were measured on an Ultima IV X-ray diffractometer (Rigaku Co.) using CuK_α radiation in the $2\theta/\theta$ scanning mode and step-scan of $\Delta(\theta) = 0.02°$. Using experimentally obtained XRD patterns, the average size of QDs was calculated using Scherrer's approach. The (2θ) and full-width at half maxima (β) of XRD peaks have been determined by fitting with linear combination of Gaussian and Lorentz functions. The instrumental contribution to the broadening of XRD peaks has been taken into account applying variance subtraction approach.

SEM images were collected using a JEOL 7800F Prime SEM. TEM selected area electron diffraction (SAED) patterns, as well as high resolution TEM (HRTEM) images were obtained using a JEOL 2100+ TEM and aberration corrected JEOL-NeoARM STEM/TEM. Diffraction patterns have been simulated using JEMS software and the TEM-SAD patterns were calibrated using Au nanoparticles as a reference. The atomic interplanar spacings were measured from selected areas of HRTEM images using fast-Fourier transform (FFT).

Spectral dependences of transmittance were measured in the spectral range from 300 nm to 1100 nm on a Cary 50 spectrophotometer (HP Co.).

Steady-state photoluminescence (PL) spectra of all the synthesized samples were recorded at room temperature on a Hitachi F4500 fluorescence spectrophotometer with a 150 W Xe lamp as a source of excitation, a diffraction grating monochromator and a photomultiplier tube detector. Excitation-emission 3D matrices (EEMs) were measured in reflection geometry. The corresponding photoluminescence excitation spectra (PLE) at relevant emission wavelengths have also been measured. PL spectra were recorded for both solid-state samples as well as NP dispersions in ethanol.

The Raman spectra were measured on a LabRam300 spectrometer by Horiba Jobin-Yvon, using the red 632.8 nm He:Ne laser line and a backscattering mode.

3. Results and discussion

3.1. Structure and morphology of the synthesized QDs

There are three phases of ternary Ag–In–S chalcogenides: $AgIn_5S_8$ and two polymorphs of $AgInS_2$. At room temperature the stable $AgInS_2$ phase is a tetragonal chalcopyrite structure type, while the high-temperature orthorhombic polymorph with a wurtzite structure type. The transition between these two phases occurs at 620 °C and $AgInS_2$ melts incongruently at 880 °C forming $AgIn_5S_8$, an In-rich phase which belongs to the cubic system and has a spinel structure. Four fifths of the In^{3+} ions are octahedrally coordinated by S^{2-} ions, while the remaining In^{3+} ions and silver ions are tetrahedrally coordinated by S^{2-} according to the general formula $(AgIn)In_4S_8$ (AB_2X_4).[71]

Structural determination by XRD and SAED of QD-55, QD-75 and QD-75US show that all synthesized particles have the spinel structure. Fig. 1a shows the reference peaks of the spinel phase $AgIn_5S_8$, which are well matched with the QD-75, showing similar peak intensity ratios indicating that QD-75 have spherical-like shape. In contrast, the QD-75US and QD-55 XRD peaks (Fig. 1c and d), are significantly broadened around the most intense (311) and (440) peaks which is due to the significant size reduction of these QDs.

Furthermore, the SAED from all QDs presented in Fig. 2 clearly show all diffraction rings associated with $AgIn_5S_8$ spinel phase, as seen by the fits of the calculated SAED with the experimental rings.

Careful analysis of the XRD (311) peak from QD-55 and QD-75US shows that there is a subtle difference in their shape (Fig. 1c and d), indicating that QD-75US has two distinct populations, as seen in Fig. 3. The larger QD-75US contribute to the narrow tip (Fig. 3a), while the population of smaller QD-75US contribute to broader tails of the (311) peak. On the other hand, a good fit of this peak for QD-55 has been obtained without a contribution of a narrow function (Fig. 3b). Two populations of QD-75US are also visible in the (440) XRD peak and, as expected, only one population for QD-55, as shown in the supplementary material, ESI Fig. 2a and b.† Utilizing the Scherrer approach, the calculated value of QD-75 average diameter is 31.2 nm. Details of the calculations are shown in ESI (ESI Fig. 3†). The average diameter of larger population of QD-75US, calculated on the basis of (311) and (440) peaks, is 19.2. Smaller QD-75US and QD-55 have average diameter less than 5 nm.

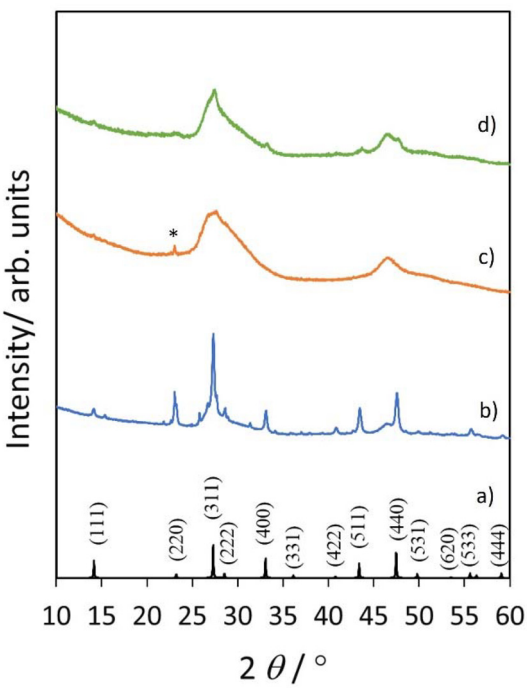

Fig. 1 XRD patterns of: (a) reference peaks for $AgIn_5S_8$, (b) QD-75, (c) QD-55 and (d) QD-75US. Reference peaks for $AgIn_5S_8$ are taken from ref. 71. The peak, appearing in (c), labeled by * is due to the polymeric sulfur.[72]

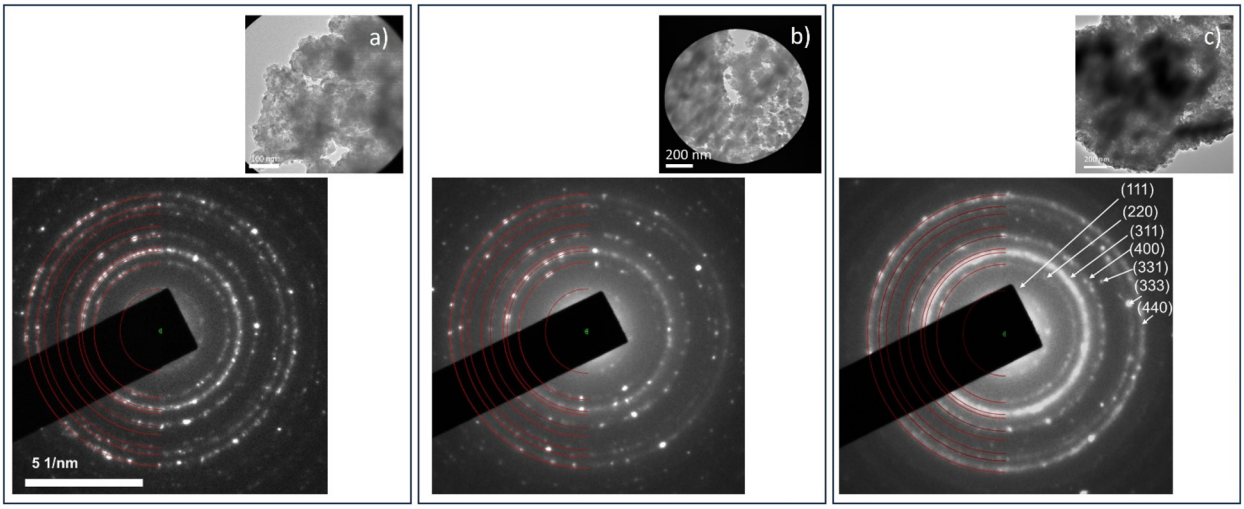

Fig. 2 SAED patterns of QD-55 (a), QD-75 (b) and QD-75US (c) with diffraction rings corresponding to $AgIn_5S_8$. The insets are BF-TEM images from the areas from which the SAED pattern were taken.

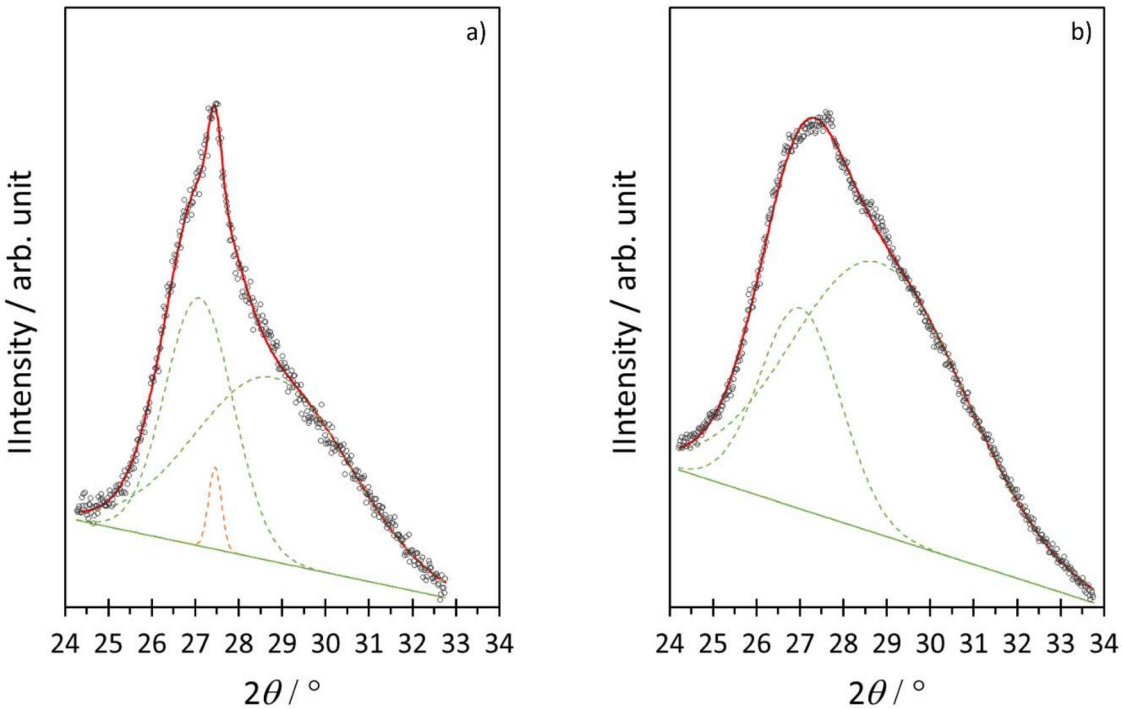

Fig. 3 (311) XRD peak of QD-75US (a) and QD-55 (b) with Gaussian fit (red line).

In order to confirm the QD size obtained by the Scherrer method, and further to study the micro and atomic structure of the QDs, TEM/STEM was performed. Fig. 4 shows low magnification images of the QDs, where the overall spherical shape of the aggregated QDs is observed. As confirmed by further HRTEM measurements, however, the aggregates are composed of distinct QDs.

The size distribution obtained by measuring their diameter, from TEM images, is shown in Fig. 5, and we observe a good agreement between average QDs size obtained by TEM and XRD. Performing a fitting procedure using a lognormal function, gives (4.9 ± 2.4) nm and (31.1 ± 9.0) nm for the average diameter of QD-55 and QD-75, respectively. For QD-75US the small and large populations are (2.6 ± 0.7) nm and (21.0 ± 3.3) nm, respectively.

Further study by TEM of QD-55 reveals fiber-like structures (Fig. 6). The fibers are due to the formation of polymeric sulfur, which are indicated in Fig. 6a and b as well as sur-

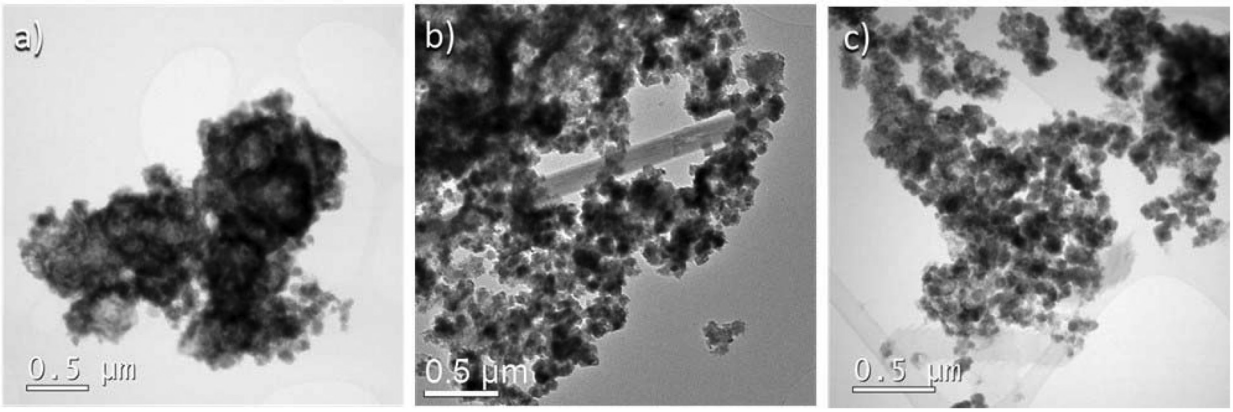

Fig. 4 STEM image of QD-55 (a), TEM image of QD-75 (b) and STEM image of QD-75US (c).

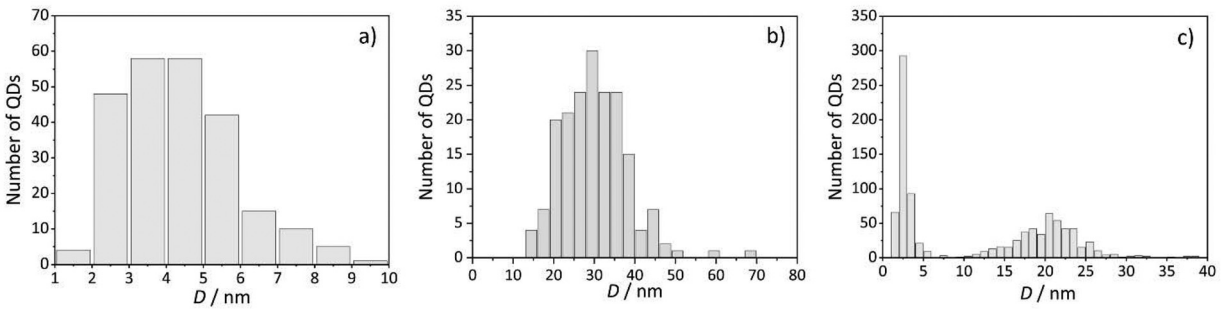

Fig. 5 The size distribution of QD-55 (a), QD-75 (b) and QD-75US (c).

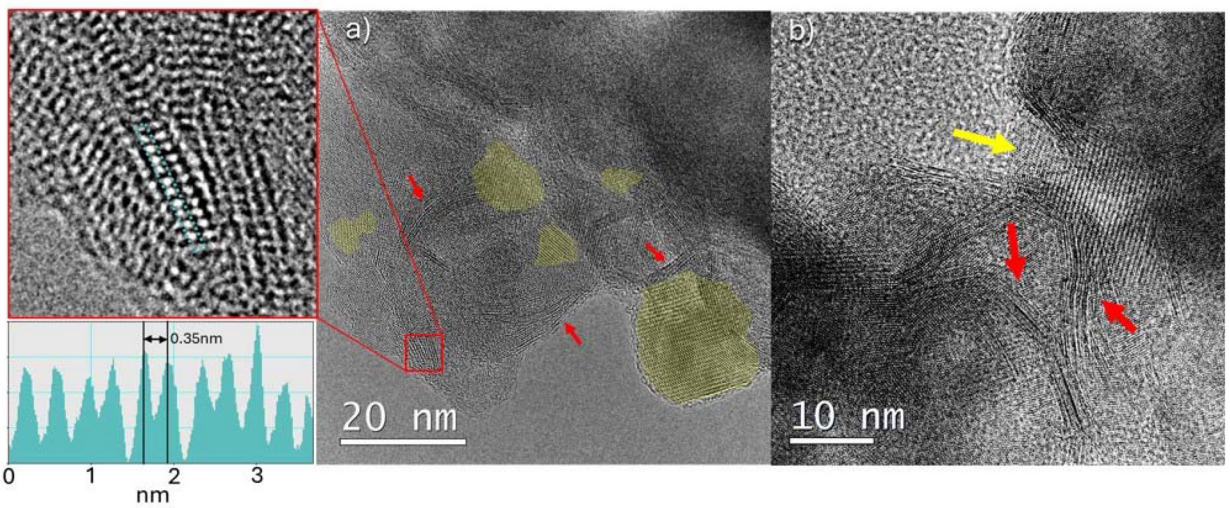

Fig. 6 STEM (a) and HRTEM (b) images of QD-55. (a) Region showing atomic lattice fringes of QD-55 (yellow shadowing). S-chains shown in the inset (left upper panel) with atomic distance of 0.35 nm obtained from intensity profile along the atomic chain. Red arrows show regions of the bundle of S-chains (a and b) and a QD indicated by the yellow arrow (b).

rounding $AgIn_5S_8$ QDs. Polymeric sulfur[72] is observed in XRD measurement (denoted with * in Fig. 1c) and using Raman spectroscopy shown in ESI Fig. 4a.† Although the peak due to polymeric sulfur seems to appear very close to the (220) reflection of $AgIn_5S_8$ QDs in the XRD pattern in Fig. 1c, a closer examination of the corresponding region clearly reveals that its position is shifted to lower 2θ values corresponding to polymeric sulfur (ESI Fig. 4b†). Comparison with literature data

reveals the Raman bands characteristic for polymeric sulfur denoted with asterisks (ESI Fig. 4b†). In addition, presence of shoulder band (denoted with red arrow) can be assigned to accretion of polymeric sulfur chains (S_μ), which indicates a certain level of disorder.[73] Note that such spectral features are absent in the Raman spectra of QD-75 and QD-75US. Atomic spacing measurements by intensity profile of HRTEM images of sulfur chains show the atom-to-atom measurements in this fiber-like structures, ~3.5 Å, that correspond to reported values of sulfur polymeric chains, Fig. 6. The excess of sulfur on reaction at 55 °C, implies that the reactants are not fully converted/consumed into the aimed final $AgIn_5S_8$ product.

The fiber structures, also illustrated by STEM imaging of QD-55 (ESI Fig. 5†), are absent for QD-75 (Fig. 7). This demonstrates that the reaction temperature significantly influences the mechanism of QD formation, resulting in formation of large QDs with average diameter of over 5 times larger than the QD-55. The HRTEM analysis of QD-75 shows that the majority have a single crystal structure (Fig. 7), which becomes polycrystalline at larger sizes, Fig. 7a. This suggests that large particles in QD-75 are likely obtained by coalescence of smaller NPs which leads to the formation of structural domains, as observed in Fig. 7a. The influence of these structural boundary defects in the QDs will influence their optical properties, as will be discussed below.

The above experimental constraints that limit controlling QDs size can be overcome using ultrasound (US) assisted synthesis. The application of US leads to free radicals such as $H^\bullet$ and $HO^\bullet$ when the cavitation medium is water (due to water homolysis), as well as reactive oxygen species which influence the precursor conversion and enhance nucleation rate.[74–76] The implosion of bubbles is nearly adiabatic and produces temperature in the thousand-degree range in the microbubbles for a very short time. This effect can be rather effective for modifying structural properties of QDs *via* local annealing effects since $AgIn_5S_8$ is characterized by relatively low melting temperature (~ 1110 °C (ref. 77)). While energy released as a consequence of the collision between QDs can invoke melting of $AgIn_5S_8$ and QD enlargement, acoustic cavitation followed by a variety of physical effects, such as shock waves and microjets, it is expected to have a dominant effect, providing a potential pathway for QD size reduction.

Indeed, the use of US enables a QD diameter reduction from (31.1 ± 9.0) nm to (2.6 ± 0.7) nm, confirming that the heterogeneous acoustic cavitation effects are dominant for QD-75US.[74,75] Furthermore, the additional minor subpopulation of QD-75US with larger size can be attributed to coalescence effects. Synthesis using US conditions also affects the crystallinity and defects of QD-75US. HRTEM shows that the majority and minority of QD-75US population histograms, shown in Fig. 5, have average diameter sizes of (2.6 ± 0.7) nm and (21.0 ± 3.3) nm respectively, with typical QDs shown in Fig. 8. The HRTEM imaging of ultrasmall QD-75US show that these NPs have single crystal structure, though even at this size range occasionally QD-75US with extended defects such as twins can be observed in ESI Fig. 6.† In contrast to QD-75, the larger population of QD-75US do not show single crystal structure, instead they show crystallographic domains (ESI Fig. 7†), indicating that they are formed *via* coalescence of smaller QDs.

3.2. Optical properties of $AgIn_5S_8$ QDs

The band gap energies of QD-55, QD-75 and QD-75US were obtained from UV-VIS spectroscopy, using a Tauc plot by extrapolating the linear region of $(\alpha h\nu)^2$ *vs.* $h\nu$ to $(\alpha h\nu) = 0$ (Fig. 9) based on the following equation for a direct dipole allowed band-to band transition:

$$h\nu = A_0\sqrt{(h\nu - E_g)} \quad (1)$$

where α is the absorption coefficient and $h\nu$ is the photon energy. The calculated band gap energies of QD-55, QD-75, and QD-75US are (3.09 ± 0.02) eV, (2.18 ± 0.01) eV and (3.77 ± 0.01) eV respectively. The band gap energies reflect the QD

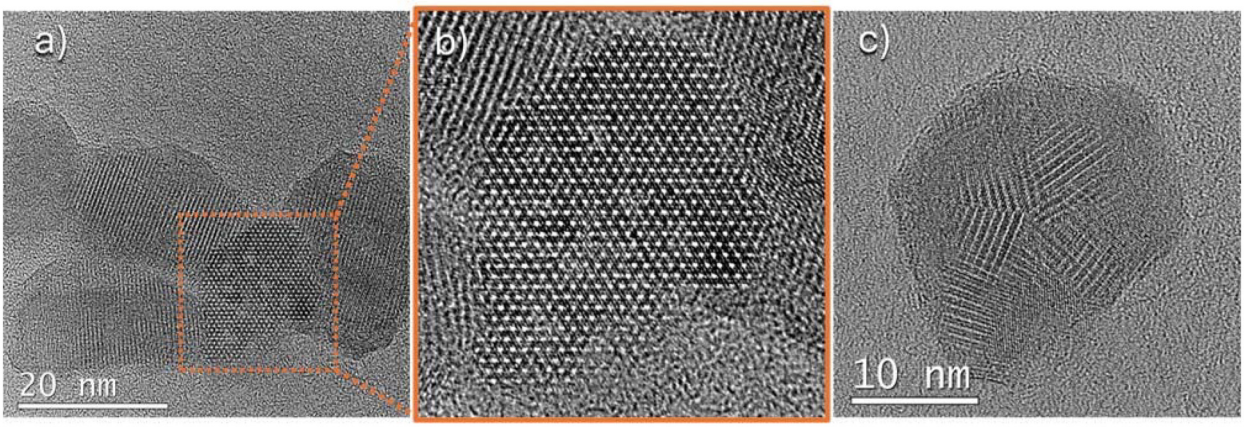

Fig. 7 (a) HRTEM of QD-75, an enlarged QD-75 is shown in (b). (c) Polycrystalline QD-75, clearly showing the structural domains and grain boundaries within a single QD-75.

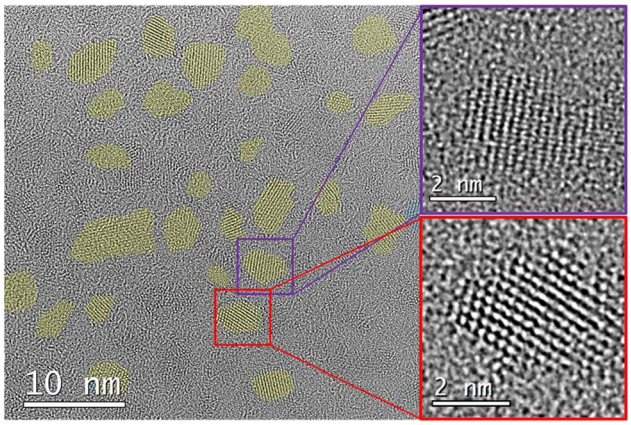

Fig. 8 HRTEM image of QD-75US whose lattice fringes are outlined by yellow shadowing color for better visibility. Two examples of HRTEM images in two different crystallographic orientations of QD-75US are shown in panels on the right.

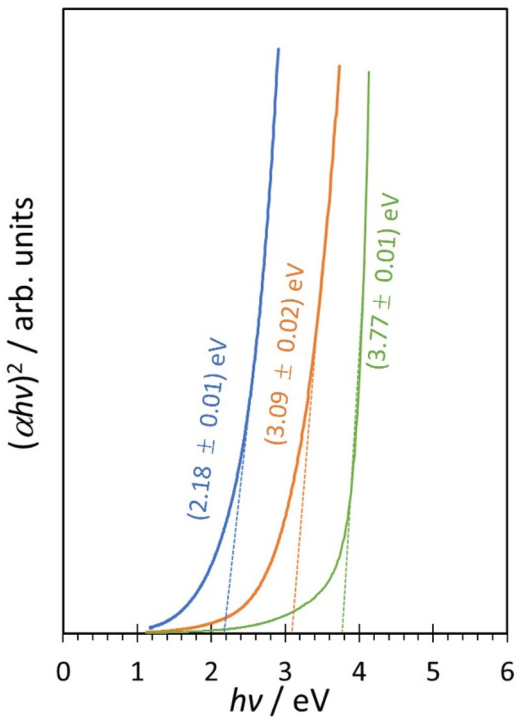

Fig. 9 $(\alpha h\nu)^2$ on $h\nu$ dependence of QD-75 (blue), QD-55 (orange) and (c) QD-75US (green). The intercepts with ($h\nu$) axis give the E_g values of the QDs.

average size with the smallest size giving the largest band gap due to the quantum confinement effect.

The >10 times reduction of the average QD diameter for QD-75US in comparison to QD-75 results in blue-shifted band gap energy for ~2 eV when compared to the bulk band gap of $AgIn_5S_8$. We note that E_g of bulk $AgIn_5S_8$ reported in the literature varies in the range between 1.7 to 1.9 eV.[78–81] Although the E_g of QD-75 is significantly red shifted with respect to QD-75US, it is still slightly blue-shifted by ~0.4 eV compared to bulk $AgIn_5S_8$, showing that quantum confinement effects are observed even for this set of particles with an average diameter of (31.1 ± 9.0) nm. We note that the theoretical study[82] of E_g confirms that the valence band maximum (VBM) and the conduction band minimum (CBM) correspond to the same point of k-space (Γ: 0.0, 0.0, 0.0), the calculated band gap value for the modelled $AgIn_5S_8$ compound (E_g = 1.2 eV) is significantly lower than the experimentally obtained values. This discrepancy is partially due to the structure of the QDs spinel phase where there is need to consider the random distribution of the 1/5 of indium ions over the tetrahedral sites along with silver ions, as well as inherent systematic errors when DFT approach is applied to excited states.

The long tail in the UV-Vis spectrum below the band gap is due to exponential sub-band gap absorption,[83–85] Fig. 11. The data from this region can be analyzed according to the Urbach–Martienssen rule:[83]

$$\alpha(h\nu, T) = \alpha_0 \cdot \exp\left(\frac{h\nu - E_0}{E_u(T, X)}\right) \quad (2)$$

where α_0 and E_0 are constants and E_u is the Urbach energy, a parameter which determines the steepness of a sub-band gap absorption tail with contributions from a temperature dependent thermal disorder (T) and inherent structural disorder (X) terms, respectively. Rearrangement of the Urbach–Martienssen rule leads to the following expression:

$$\ln(\alpha) = \left[\ln(\alpha_0) - \frac{E_0}{E_u}\right] + \frac{1}{E_u}E \quad (3)$$

The values of Urbach energy, obtained from the slope of lnα on photon energy dependences of QD-75US, QD-55 and QD-75 (Fig. 10), are (916 ± 56) meV, (1097 ± 37) meV and (1271 ± 22) meV respectively. The smallest Urbach energy value of QD-75US implies that the US-assisted route leads towards a lower degree of inherent structural disorder compared to the QDs synthesized under purely thermal conditions. These data correlate with HRTEM analysis (Fig. 7), where the structure of QD-75 is less-ordered compared to the QD-75US, clearly showing structural domains separated by the grain boundaries that deviate from ideal bulk atomic stacking. It is also expected that the minor population of large QD-75US would also affect the sub-band gap absorption albeit below the region of Urbach absorption of the smaller QDs, due to its lower E_g.

The different band gap (E_g) and Urbach (E_u) energies arising from size and structural differences are expected to significantly influence the PL properties of the $AgIn_5S_8$ QDs and have been probed using excitation-emission steady-state photoluminescence (PL). The relevant regions of the PL spectra of the QDs are shown in Fig. 11 as contour plots. Upon elimination of the first-, second- and third-order Rayleigh scattering and Raman scattering features, the persistent PL features were analyzed and assigned. In this section, the focus is on emission bands due to band-to-band electronic transitions.

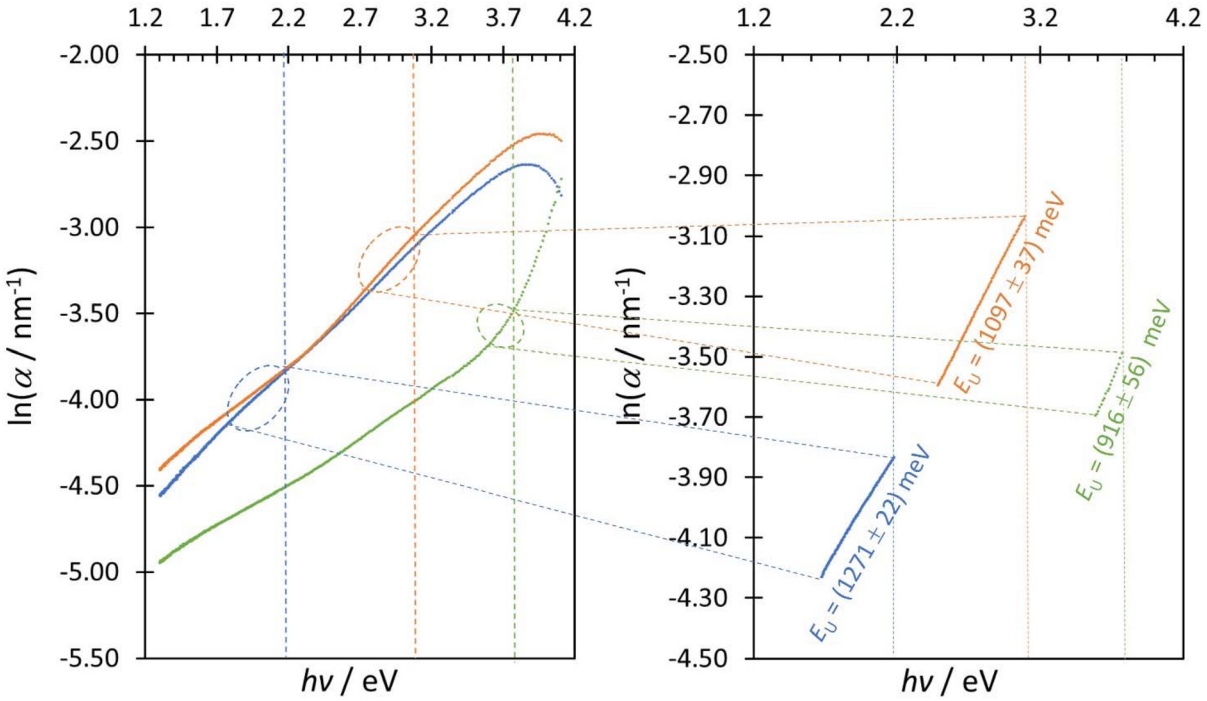

Fig. 10 Left panel shows ln α on *hv* dependences of QD-55 (orange), QD-75 (blue) and QD-75US (green). Right panel shows lnα on *hv* dependences of QD-55 (orange), QD-75 (blue) and QD-75US (green) in the sub-band gap absorption regime.

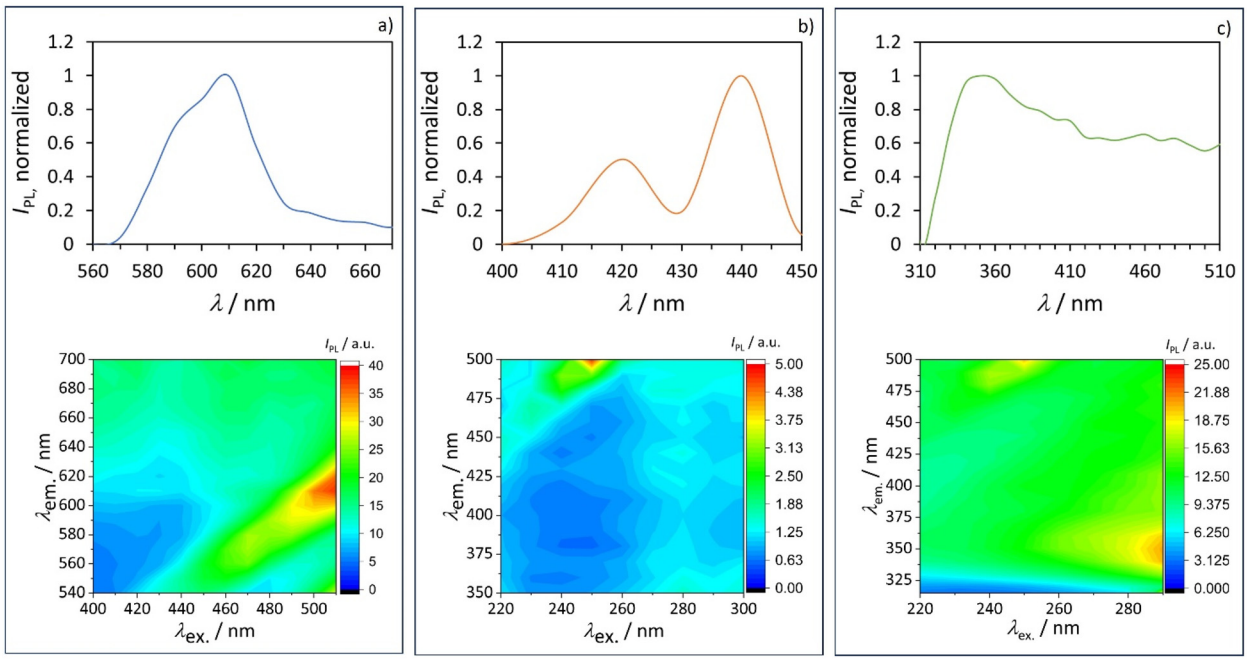

Fig. 11 Relevant regions of the excitation-emission steady-state PL spectra (3D excitation-emission matrices – EEMs) represented as contour plots (lower panels) together with the corresponding PL spectra obtained as slices through the EEM at excitation wavelengths (upper panels) at 500, 280 and 280 nm for: (a) QD-75, (b) QD-55 and (c) QD-75US, respectively.

Fig. 11a shows the PL spectrum of QD-75 obtained as a slice through the 3D plot at an excitation wavelength of 500 nm. The PL spectrum is dominated by an intense emission band at ~610 nm (2.03 eV) and a satellite band at ~590 nm (2.10 eV), see ESI Fig. 8a.† The transition energies of both bands lie slightly lower in energy than the band gap

energy determined from absorption spectroscopy. We attribute this finding to the adiabatic optical absorption–induced interband electronic transition which leads directly to an excited vibrational state(s) within the excited electronic state, according to the Franck–Condon principle. The corresponding interband transition due to emission, on the other hand, starts from the ground vibrational state of the excited electronic state of the QD and leads to an excited vibrational state within the ground electronic state and thus occurs at lower energy than the transition due to optical absorption.

Fig. 11b, at an excitation wavelength of 280 nm of QD-55, shows two dominant Gaussian-type emission bands at ~420 nm (2.95 eV) and ~440 nm (2.82 eV). Both transition energies are, again, somewhat below the optical band gap energy of 3.1 eV. We attribute the higher – energy (2.95 eV) PL band to the band-to-band recombination emission. The lower energy band (2.82 eV), with higher PL intensity, is attributed to the recombination involving shallow band gap states located near the conduction or valence band edges.

Fig. 11c shows the PL spectrum of QD-75US obtained at excitation wavelength of 280 nm. The centroid of the lowest-wavelength emission band in this case appears at ~350 nm (3.54 eV), slightly below the optical band gap value determined from analysis of the absorption spectroscopy data (3.77 eV). This band is notably structured from the higher-wavelength side, although these features are intensity-amplified by the band due to second-order Rayleigh scattering band appearing at doubled excitation frequency (560 nm).

The static PL data (concerning band-to-band emission wavelengths) are in excellent correlation with the band gap energies corresponding to fundamental band-to-band transitions computed from the optical absorption spectra. Fig. 12 shows the superimposed optical absorption and photoluminescence spectra of QD-55 and QD-75US. Positions of the PL band maxima are plotted *vs.* the corresponding optical band gap energies in ESI Fig. 8b.† Particularly, the shifts in band-to-band emission energies in the series QD-75, QD-55 and QD-75US, obtained from the static PL spectra are in excellent agreement with the shifts in optical band gap energies, which further confirms the correct assignments and claims outlined before in the manuscript (ESI – Table 1†). It is important to note that the half-widths of the PL bands are about 100 meV in the case of QD-75. As shown in the next chapter, they are significantly narrowed upon thermal annealing treatment. These values are, however, already comparable to those which are considered as industry standards.[63,64]

3.3. Structural and optical properties of annealed $AgIn_5S_8$ QDs

The above data clearly show the dependence of optical properties on the size and structural defects of the QDs. Next, we explore how improving the structural properties of all 3 sets reflects to their functional properties. Annealing is a standard procedure to improve crystallinity, grow structural domains and remove grain boundaries *via* sintering. The as-synthesized QDs annealing at 100 °C and 200 °C for 1 h does not change the band gap or the Urbach energy of the QDs implying that this treatment does not significantly affect their size and degree of structural disorder. Upon annealing at 200 °C for 2 h, the absorption of the QDs was modified, as seen from the spectral dependences of the absorption coefficient α, orange curve in Fig. 13, showing the transition from QD to bulk like behavior of $AgIn_5S_8$. Consequently, the band gap energy of all

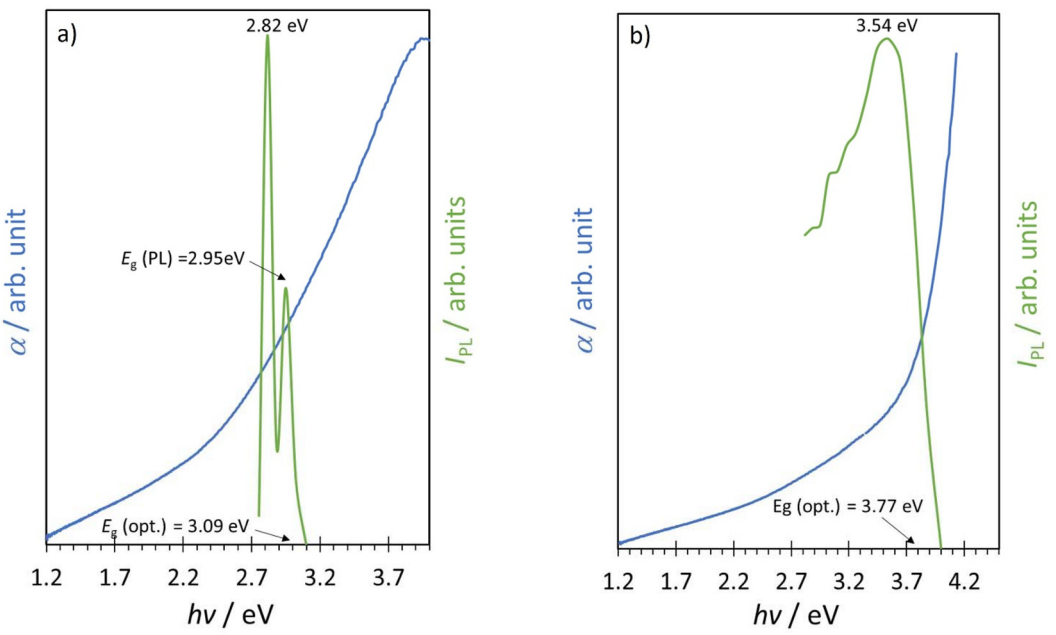

Fig. 12 Superimposed optical absorption and photoluminescence spectra of QD-55 (a) and QD-75US (b).

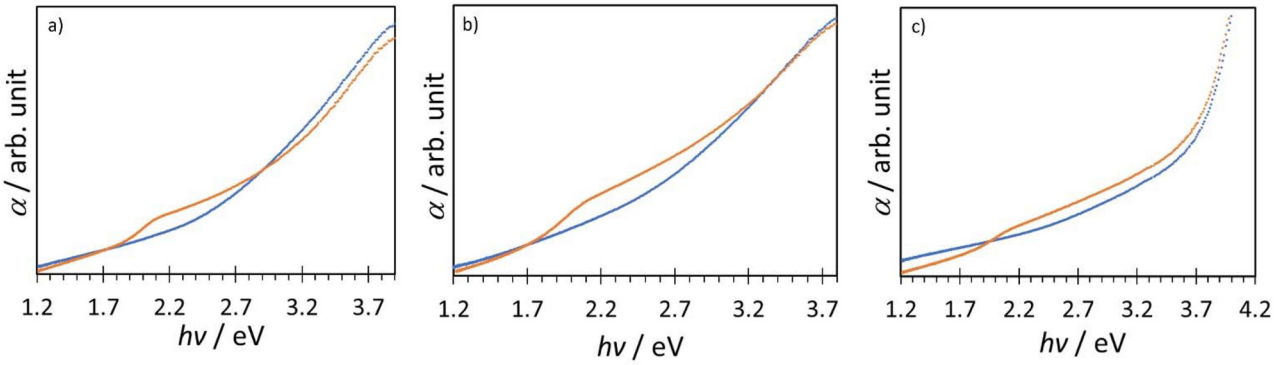

Fig. 13 Spectral dependences of absorption coefficient (a) QD-55, (b) QD-75 and (c) QD-75US of unannealed QDs (blue) and annealed QDs at 200 °C for 2 h (orange), respectively.

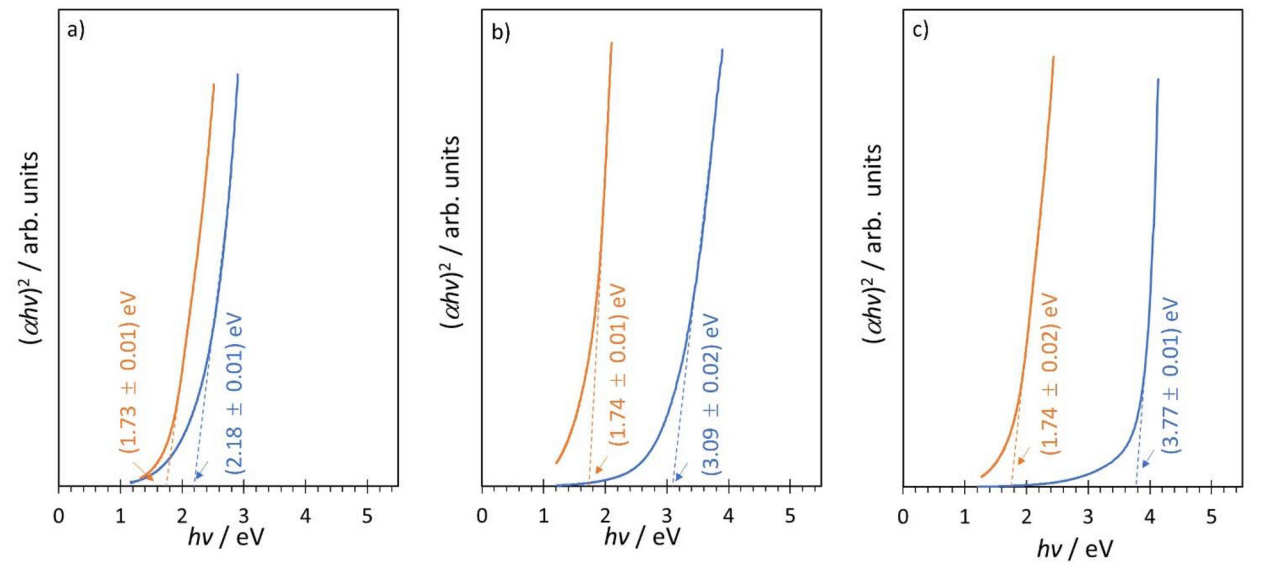

Fig. 14 $(\alpha h\nu)^2$ *vs. hν* dependence of (a) QD-75, (b) QD-55 and (c) QD-75US unannealed (blue) and annealed at 200 °C for 2 h (orange), respectively.

QDs, upon annealing at 200 °C for 2 h, has reached the bulk values of 1.74 eV, Fig. 13.

The red-shifted band gap energy (Fig. 14) indicates QDs enlargement due to sintering upon annealing, as well as different population sizes before and after thermal treatment. The increase in QD size and overall crystallinity has been confirmed by XRD (ESI Fig. 9†) and TEM measurements. The XRD peaks become narrower and clearly defined particularly in comparison to the smaller QD-55 and QD-75US. The average size of all QDs increased with QD-55 and QD-75 giving diameters of 33.5 nm and 33.9 nm respectively, while QD-75US gives 23.3 nm (ESI Fig. 10†). While convergence of the E_g of all QDs towards the bulk band gap value of $AgIn_5S_8$ is found, the Urbach energies significantly decreased only for QD-75, from (1271 ± 22) meV to (855 ± 5) meV (Fig. 14 and Table 1).

In contrast the Urbach energy for QD-55 and QD-75US remains similar (Fig. 15). The experimentally found Urbach energies suggest different levels of structural/chemical ordering between the QD-75 and QD-55/QD-75US. As seen from the table the Urbach energies for QD-55 and QD-75US remain the same within the experimental error before and after the annealing, indicating less ordered structure of these QDs after the annealing process in comparison to QD-75.

Table 1 Band gap energy (E_g) and Urbach energy (E_U) of unannealed and annealed QDs at 200 °C for 2 h

		E_g/eV	E_u/meV
QD-55	Unannealed	3.09 ± 0.02	1097 ± 37
	Annealed	1.74 ± 0.01	1023 ± 19
QD-75	Unannealed	2.18 ± 0.01	1271 ± 22
	Annealed	1.73 ± 0.01	855 ± 5
QD-75US	Unannealed	3.77 ± 0.01	916 ± 56
	Annealed	1.74 ± 0.02	990 ± 44

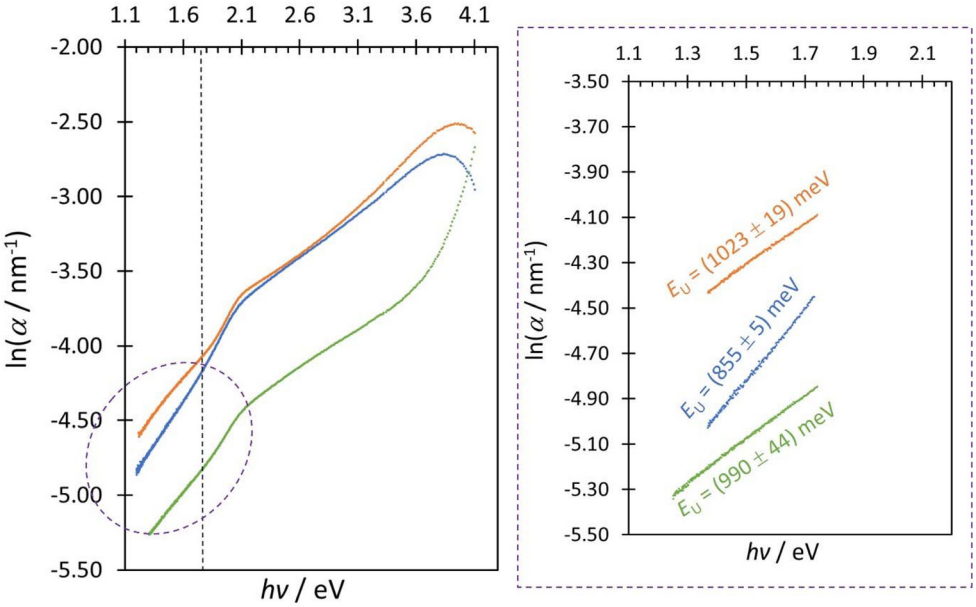

Fig. 15 Left panel shows lnα on *hv* dependences of QD-55 (orange), QD-75 (blue) and QD-75US (green). Right panel shows lnα on *hv* dependences of QD-55 (orange), QD-75 (blue) and QD-75US (green) in the sub-band gap absorption regime.

Indeed, a difference in structural ordering has been observed by HRTEM after annealing (Fig. 16). While overall improvement of QD crystallinity is observed, QD-55 shows an increase in stacking faults between the large crystalline grains, as well as multiple grain boundaries within single QDs (Fig. 16a). These extended defects are less present in annealed

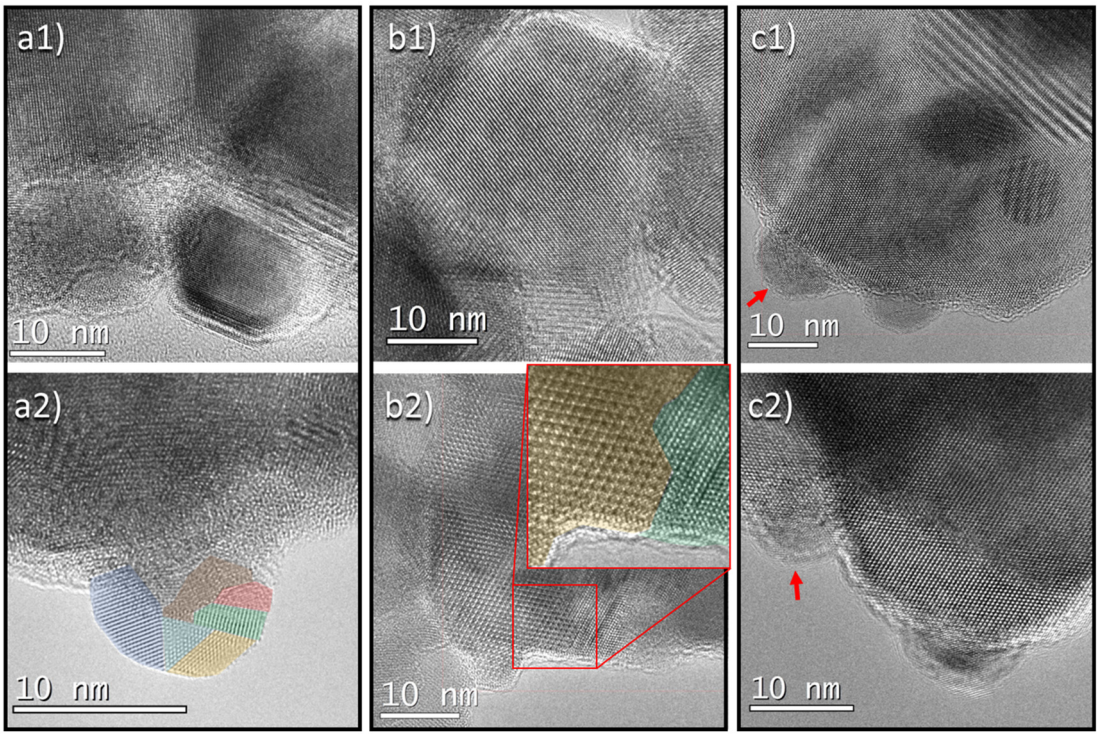

Fig. 16 TEM images of QDs after annealing at 200 °C for 2 h. (a1) QD-55 showing large crystal domains separated by regions with defects; (a2) multistructural domains in smaller QDs outlined by different shading colors. (b1) QD-75 showing large crystalline regions with grain boundaries present between them as shown by the highlighted stacking fault region in (b2). (c1) and (c2) show QD-75US where large crystalline domains as well as small QDs are observed, arrows point to regions where structural disorder is present.

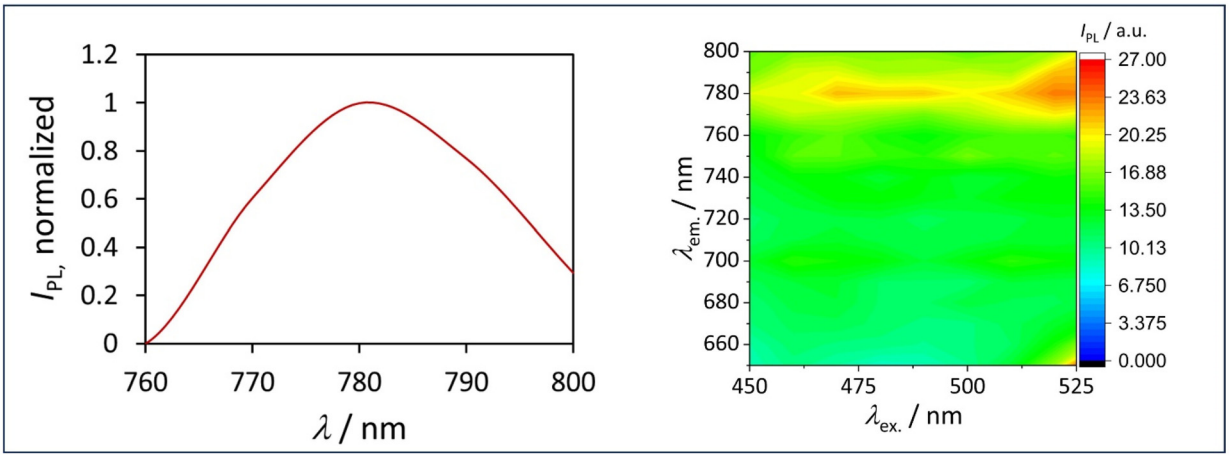

Fig. 17 Excitation-emission steady-state PL spectrum of QD-75 annealed at 200 °C for 2 h represented as contour plot (right panel) and the corresponding PL spectrum at 500 nm excitation wavelengths (left panel).

QD-75US, and we note also the presence of a population of small QD-75US (Fig. 16c), which likely is the main contributor of overall structural disorder in these QDs. In the case of QD-75, the number of grain boundaries and stacking faults is decreased, though occasionally twin defects and other type of defects are present (Fig. 16b). The structural analysis of annealed QDs show that there is correlation between the ordering and initial QD size, implying that annealing of small QDs population drives coalescence and overall improvement of crystallinity. However, for QD-55 and QD-75US the presence of extended defects is the main cause of unchanged Urbach energies before and after annealing at the chosen conditions. In contrast, the large size of QD-75 and relatively good crystallinity before annealing (Fig. 1b), shows that the annealing process helps to improve structural/chemical ordering (with only small change in size of ~3 nm), reflected in a change of the band gap of 0.4 eV and decrease of the Urbach energy of ~400 meV.

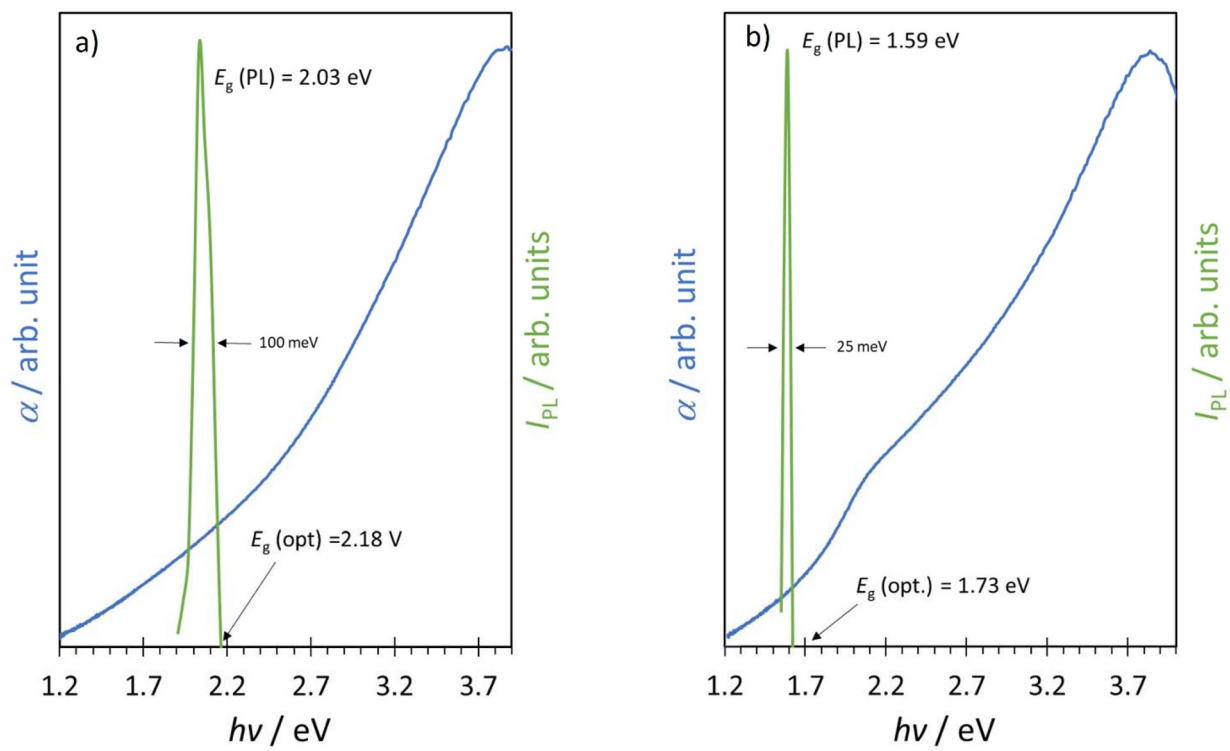

Fig. 18 Superimposed optical absorption and photoluminescence spectra of QD-75, unannealed (a) and annealed (b).

We note that additional annealing of QD-55 and QD-75 for 2 h was not followed by further decrease of band gap energy, the bulk value of E_g has been already reached upon annealing at the mentioned temperature for 2 h (Table 1).

It is important to mention in this context that I–III–VI QDs have been also shown to exhibit notable tunability of the band gap energy upon doping, too (see, *e.g.* ref. 86).

The effect of post-synthetic annealing on the PL properties can be seen from Fig. 17 where excitation wavelength of 520 nm for annealed QD-75 shows a single emission band at ~780 nm (1.59 eV), as compared to the band gap energy calculated from optical spectroscopy data of 1.73 eV. This band is evidently much less structured than the bands observed in the as synthesized QD-75 attributable to the more uniform QDs size distribution in this case. Fig. 18 shows the superimposed optical absorption and photoluminescence spectra of as-deposited and annealed QD-75, respectively. The decrease of FWHM of the PL band is evident, the final value of this parameter converging to ~25 meV in the case of QD-75 annealed samples. To summarize the results concerning this aspect, in stark contrast to previous reports on I–III–VI nanomaterials, our QDs exhibit sharp, band-edge emission, with PL band half-widths which are within or better than industrial standards, and notably better than those of typical II–VI QDs such as CdSe, CdTe, and InP.[63,64] This clearly indicates high compatibility of the presently synthesized material with the industry standards.

4. Conclusions

In this study, we have successfully synthesized spinel $AgIn_5S_8$ quantum dots (QDs) using a colloidal bottom-up approach. At 55 °C, the chemical reaction leads to the simultaneous formation of small QDs and sulfur polymer chains, which restrict QD growth to an average diameter of (4.9 ± 2.4) nm and a corresponding band gap energy of (3.09 ± 0.02) eV. Raising the reaction temperature to 75 °C suppresses sulfur-chain formation, which leads to larger QDs formation with an average size of (31.1 ± 9.0) nm, and a reduced band gap of (2.18 ± 0.01) eV. Introducing US irradiation at 75 °C effectively limits QD growth, yielding a dominant population of ultrasmall QDs with an average size of (2.6 ± 0.7) nm and a wide band gap of (3.77 ± 0.01) eV.

Thermal annealing of the QDs synthesizes at 55 and 75 °C (QD-55 and QD-75), for 2 h at 200 °C, increases their size to ~34 nm, while the QD-75US reaches a smaller post-annealing size of ~23 nm. All annealed QDs exhibit a band gap energy approaching the bulk value of ~1.7 eV.

The achieved size range—from 2.6 nm to 34 nm—enables an unprecedented degree of band gap tunability for a ternary Ag-based system, spanning a range from 1.70 eV to 3.77 eV *i.e.* approximately 2 eV across the visible spectrum, demonstrating the remarkable potential of the $AgIn_5S_8$ system.

Photoluminescence (PL) measurements reveal a strong correlation between emission characteristics and QD structure and size. Crucially, in stark contrast to previous reports on I–III–VI nanomaterials, our QDs exhibit sharp, band-edge emission. The FWHM is as narrow as ~25 meV for annealed samples, a value that is several times lower than that of industry-standard II-VI QDs (*e.g.*, CdSe, InP) and well within the stringent requirements for high-definition displays.

While XRD and electron diffraction confirm the cubic spinel structure in all cases, HRTEM uncovers varying degrees of structural ordering. Larger QDs formed *via* coalescence exhibit multiple structural domains and grain boundaries, contributing to increased Urbach energies in as-prepared samples. Annealing improves structural ordering most significantly in QD-75, where initial and post-annealing sizes are similar. In contrast, QD-55 and QD-75US undergo considerable coalescence during annealing, forming new grain boundaries and stacking faults which essentially do not change their Urbach energies.

Overall, this work highlights $AgIn_5S_8$ QDs as a highly versatile material platform with exceptional band gap tunability. Further improvements in photophysical properties are anticipated through strategies such as doping and surface passivation. These enhancements, combined with the inherent biocompatibility and non-toxicity of $AgIn_5S_8$, position this system as a strong candidate for optoelectronic and biomedical applications. This study therefore provides key insights into structure–property relationships and low-cost wet-chemical strategies for $AgIn_5S_8$ QD synthesis.

Conflicts of interest

There are no conflicts to declare.

Data availability

The datasets generated and analyzed during the current study are available from the authors on reasonable request.

References

1 E. Jang and H. Jang, Quantum Dot Light-Emitting Diodes, *Chem. Rev.*, 2003, **123**, 4663–4692.
2 M. A. Cotta, Quantum Dots and Their Applications: What Lies Ahead?, *ACS Appl. Nano Mater.*, 2020, **3**, 4920–4924.
3 A. L. Efros and L. E. Brus, Nanocrystal Quantum Dots: From Discovery to Modern Development, *ACS Nano*, 2021, **15**, 6192–6210.
4 F. P. García de Arquer, V. Dmitri, V. D. Talapin, I. Klimov, Y. Arakawa, M. Bayer and E. H. Sargent, Semiconductor quantum dots: Technological progress and future challenges, *Science*, 2021, **373**, 640–654.
5 M. Bayer, Bridging Two Worlds: Colloidal versus Epitaxial Quantum Dots Manfred Bayer, *Ann. Phys.*, 2019, 1900039–1900064.

6 A. I. Ekomov and A. A. Onushchenko, Quantum size effects in three-dimensional microscopic semiconductor crystals, *JETP Lett.*, 1981, **34**, 363–366.
7 R. Rossetti, S. Nakahara and L. E. Brus, Quantum size effects in the redox potentials, resonance Raman spectra, and electronic spectra of CdS crystallites in aqueous solution, *J. Chem. Phys.*, 1983, **79**, 1086–1088.
8 L. Brus, Electronic wave functions in semiconductor clusters: Experiment and theory, *J. Phys. Chem.*, 1986, **90**, 2555–2560.
9 A. P. Alivisatos, A. L. Harris, N. J. Levinos, M. L. Steigerwald and L. E. Brus, Electronic states of semiconductor clusters: Homogeneous and inhomogeneous broadening of the optical spectrum, *J. Chem. Phys.*, 1988, **89**, 4001–4011.
10 J. Sobhanan, J. V. Rival, A. Anas, E. S. Shibu, Y. Takano and V. Biju, Luminescent quantum dots: Synthesis, optical properties, bioimaging and toxicity, *Adv. Drug Delivery Rev.*, 2023, **197**, 114830 (35 pages).
11 K. Zarschler, L. Rocks, N. Licciardello, L. Boselli, E. Polo, K. P. Garcia, L. D. Cola, H. Stephan and K. A. Dawson, Ultrasmall inorganic nanoparticles: State-of-the-art and perspectives for biomedical applications, *Nanomedicine*, 2016, **12**, 1663–1701.
12 A. Delices, D. Moodelly, C. Hurot, Y. Hou, W. L. Ling, C. Saint-Pierre, D. Gasparutto, G. Nogues, P. Reiss and K. Kheng, Aqueous Synthesis of DNA-Functionalized Near-Infrared $AgInS_2$/ZnS Core/Shell Quantum Dots, *ACS Appl. Mater. Interfaces*, 2020, **12**, 44026–44038.
13 L. Boselli, E. Polo, V. Castagnola and K. A. Dawson, Regimes of biomolecular ultrasmall nanoparticle interactions, *Angew. Chem., Int. Ed.*, 2017, **56**, 4215–4218.
14 M. Epple, V. M. Rotello and K. Dawson, The Why and How of Ultrasmall Nanoparticles, *Acc. Chem. Res.*, 2023, **56**(23), 3369–3378.
15 C. B. Murray, D. J. Norris and M. G. Bawendi, Synthesis and characterization of nearly monodisperse CdE (E = sulfur, selenium, tellurium) semiconductor nanocrystallites, *J. Am. Chem. Soc.*, 1993, **115**, 8706–8715.
16 F. W. Wise, Lead salt quantum dots: The limit of strong quantum confinement, *Acc. Chem. Res.*, 2000, **33**, 773–780.
17 C. B. Murray, C. R. Kagan and M. G. Bawendi, Synthesis and characterization of monodisperse nanocrystals and close-packed nanocrystal assemblies, *Annu. Rev. Mater. Sci.*, 2000, **30**, 545–610.
18 M. C. Weidman, M. E. Beck, R. S. Hoffman, F. Prins and W. A. Tisdale, Monodisperse, air-stable PbS nanocrystals via precursor stoichiometry control, *ACS Nano*, 2014, **8**, 6363–6371.
19 X. Zheng, Y. Liu, Y. Yang, Y. Song, P. Deng, J. Li, W. Liu, Y. Shen and X. Tian, Recent Advances in Cadmium Sulfide-Based Photocatalysts for Photocatalytic Hydrogen Evolution, *Renewables*, 2023, **1**, 39–56.
20 W. M. Girma, M. Z. Fahmi, A. Permadi, M. A. Abate and J. Y. Chang, Synthetic Strategies and Biomedical Applications of I–III–VI Ternary Quantum Dots, *J. Mater. Chem. B*, 2017, **5**, 6193–6216.
21 H. Zhong, Z. Bai and B. Zou, Tuning the Luminescence Properties of Colloidal I–III–VI Semiconductor Nanocrystals for Optoelectronics and Biotechnology Applications, *J. Phys. Chem. Lett.*, 2012, **3**, 3167–3175.
22 D. Aldakov, A. Lefrançois and P. Reiss, Ternary and Quaternary Metal Chalcogenide Nanocrystals: Synthesis, Properties and Applications, *J. Mater. Chem. C*, 2013, **1**, 3756–3776.
23 Z. Bai, W. Ji, D. Han, L. Chen, B. Chen, H. Shen, B. Zou and H. Zhong, Hydroxyl-Terminated $CuInS_2$ Based Quantum Dots: Toward Efficient and Bright Light Emitting Diodes, *Chem. Mater.*, 2016, **28**, 1085–1091.
24 N. Tsolekile, S. Nahle, N. Zikalala, S. Parani, E. H. M. Sakho, O. Joubert, M. C. Matoetoe, S. P. Songca and O. S. Oluwafemi, Cytotoxicity, Fluorescence Tagging and Gene-Expression Study of $CuInS_2$/ZnS QDS - Meso (Hydroxyphenyl) Porphyrin Conjugate against Human Monocytic Leukemia Cells, *Sci. Rep.*, 2020, **10**, 4936 (10 pages).
25 P. Reiss, M. Carrière, C. Lincheneau, L. Vaure and S. Tamang, Synthesis of Semiconductor Nanocrystals, Focusing on Nontoxic and Earth-Abundant Materials, *Chem. Rev.*, 2016, **116**, 10731–10819.
26 B. Mao, C. H. Chuang, J. Wang and C. Burda, Synthesis and Photophysical Properties of Ternary I_III_VI $AgInS_2$ Nanocrystals: Intrinsic versus Surface States, *J. Phys. Chem. C*, 2011, **115**, 8945–8954.
27 Y. Linxiang, Z. Shuai, X. Bo, J. Jiangyuan, C. Bo, L. Xinyi, Z. Yousheng, F. Zhiyong, Y. Heesun and Z. Haibo, I-III-VI Quantum Dots and Derivatives: Design, Synthesis, and Properties for Light-Emitting Diodes, *Nano Lett.*, 2023, **23**(7), 2443–2453.
28 X. Xie, J. Zhao, O. Lin, Z. Yin, X. Li, Y. Zhang and A. Tang, Narrow-Bandwidth Blue-Emitting Ag-Ga-Zn-S Semiconductor Nanocrystals for Quantum-Dot Light-Emitting Diodes, *J. Phys. Chem. Lett.*, 2022, **13**(51), 11857–11863.
29 E. C. Hansen, Y. Liu, H. Utzat, S. N. Bertram, J. C. Grossman and M. G. Bawendi, Blue Light Emitting Defective Nanocrystals Composed of Earth-Abundant Elements, *Angew. Chem., Int. Ed.*, 2020, **59**(2), 860–867.
30 C. Giansante and I. Infante, Surface Traps in Colloidal Quantum Dots: A Combined Experimental and Theoretical Perspective, *J. Phys. Chem. Lett.*, 2017, **8**, 5209–5215.
31 X. Li, L. Wang, D. Wei, S. Kang and J. Mu, One-pot synthesis and visible light photocatalytic activity of monodispersed $AgIn_5S_8$ microspheres, *Mater. Res. Bull.*, 2013, **48**, 286–289.
32 Y. Li, Y. Liu, G. Gao, Y. Zhu, D. Wang, M. Ding, T. Yao, M. Liu and W. You, L-cysteine and urea synergistically-mediated one-pot one-step self-transformed hydrothermal synthesis of *p*-Ag_2S/*n*-$AgInS_2$ core-shell heteronanoflowers for photocatalytic MO degradation, *Appl. Surf. Sci.*, 2021, **548**(149279), 13.
33 Q. Zhang, M. Wang, M. Ao, Y. Luo, A. Zhang, L. Zhao, L. Yan, F. Deng and X. Luo, Solvothermal synthesis of

Z-scheme $AgIn_5S_8/Bi_2WO_6$ nano-heterojunction with excellent performance for photocatalytic degradation and Cr(VI) reduction, *J. Alloys Compd.*, 2019, **805**, 41–49.

34 L. H. Lin, C. C. Wu and T. C. Lee, Growth of crystalline $AgIn_5S_8$ thin films on glass substrates from aqueous solutions, *Cryst. Growth Des.*, 2007, **7**, 2725–2732.

35 X. W. Xu, F. Deng, P. H. Shao, D. D. Dionysiou, X. B. Luo, X. B. Li, S. Q. Zhang, X. G. Liu and M. Liu, Internal electric field driving separation and migration of charge carriers via Z-scheme path in $AgIn_5S_8$/ZnO heterojunction for efficient decontamination of pharmaceutical pollutants, *Chem. Eng. J.*, 2022, **428**(132096), 12.

36 D. Chen and J. Ye, Photocatalytic H_2 evolution under visible light irradiation on $AgIn_5S_8$ photocatalyst, *J. Phys. Chem. Solids*, 2007, **68**, 2317–2320.

37 F. Deng, L. Zhao, X. Luo, S. Luo and D. D. Dionysiou, Highly efficient visible-light photocatalytic performance of Ag/$AgIn_5S_8$ for degradation of tetracycline hydrochloride and treatment of real pharmaceutical industry wastewater, *Chem. Eng. J.*, 2018, **333**, 423–433.

38 W. S. Chang, C. C. Wu, M. S. Jeng, K. W. Cheng, C. M. Huang and T. C. Lee, Ternary Ag-In-S polycrystalline films deposited using chemical bath deposition for photoelectrochemical applications, *Mater. Chem. Phys.*, 2010, **120**, 307–312.

39 Y. Sun, L. Zhang, Y. Lv, Q. Zeng, X. Guo, W. Ji and X. Liu, Highly Stable Core/Shell $AgIn_5S_8$/ZnS Quantum Dots for Pure White Light-Emitting Diodes, *ACS Appl. Nano Mater.*, 2023, **6**, 22311–22319.

40 D. Zhang, W. Cao, B. Mao, Y. Liu, F. Li, W. Dong, T. Jiang, Y. C. Yong and W. Shi, Efficient 0D/2D Heterostructured Photocatalysts with Zn-$AgIn_5S_8$ Quantum Dots Embedded in Ultrathin NiS Nanosheets for Hydrogen Production, *Ind. Eng. Chem. Res.*, 2020, **59**, 16249–16257.

41 G. Gong, Y. Liu, B. Mao, B. Wang, L. Tan, D. Li, Y. Liu and W. Shi, Mechanism study on the photocatalytic efficiency enhancement of MoS_2 modified Zn–$AgIn_5S_8$ quantum dots, *RSC Adv.*, 2016, **6**, 99023–99033.

42 S. Song, Z. Liang, W. Fu and T. Peng, Preparation of Single-Crystalline $AgIn_5S_8$ Octahedrons with Exposed {111} Facets and Its Visible-Light-Responsive Photocatalytic H_2 Production Activity, *ACS Appl. Mater. Interfaces*, 2017, **9**, 17013–17023.

43 S. Jeong, H. C. Yoon, N. S. Han, J. H. Oh, S. M. Park, B. K. Min, Y. R. Do and J. K. Song, Band-Gap States of $AgIn_5S_8$ and ZnS–$AgIn_5S_8$ Nanoparticles, *J. Phys. Chem. C*, 2017, **121**, 3149–3155.

44 S. P. Hong, H. K. Park, J. H. Oh, H. Yangb and Y. R. Do, Comparisons of the structural and optical properties of o-$AgInS_2$, t-$AgInS_2$, and c-$AgIn_5S_8$ nanocrystals and their solid-solution nanocrystals with ZnS, *J. Mater. Chem.*, 2012, **22**, 18939–18949.

45 N. S. Han, H. C. Yoon, S. Jeong, J. H. Oh, S. M. Park, Y. R. Do and J. K. Song, Origin of highly efficient photoluminescence in $AgInS_2$ nanoparticles, *Nanoscale*, 2017, **9**, 10285–10291.

46 P. Sharma, A. Kumar, G. Zheng, T. Mashifana, P. Dhiman, G. Sharma and F. J. Stadler, Current scenario in ternary metal indium sulfides-based heterojunctions for photocatalytic energy and environmental applications, *Mater. Today Commun.*, 2023, **36**, 106741 (28 pages).

47 Q. Zhou, Y. Huang, Y. Zhang, C. Xu, W. Huang, K. Yang, X. Chen and Y. Zhang, Insight into the growth mechanism of $AgIn_5S_8$ nanoparticles in a low temperature co-precipitation process and their visible-light-driven photocatalytic activities, *Mater. Chem. Phys.*, 2022, **276**, 125333 (10 pages).

48 T. Torimoto, T. Adachi, K. I. Okazaki, M. Sakuraoka, T. Shibayama, B. Ohtani, A. Kudo and S. Kuwabata, Facile synthesis of ZnS-$AgInS_2$ solid solution nanoparticles for a color-adjustable luminophore, *J. Am. Chem. Soc.*, 2007, **129**(41), 12388.

49 M. L. Dai, S. Ogawa, T. Kameyama, K. Okazaki, A. Kudo, S. Kuwabata, Y. Tsuboi and T. Torimoto, Tunable photoluminescence from the visible to near-infrared wavelength region of nonstoichiometric $AgInS_2$ nanoparticles, *J. Mater. Chem.*, 2012, **22**(25), 12851–12858.

50 L. W. Liu, R. Hu, W. C. Law, I. Roy, J. Zhu, L. Ye, S. Y. Hu, X. H. Zhang and K. T. Yong, Optimizing the synthesis of red- and near-infrared $CuInS_2$ and $AgInS_2$ semiconductor nanocrystals for bioimaging, *Analyst*, 2013, **138**(20), 6144–6153.

51 T. Chen, X. B. Hu, Y. Q. Xu, L. J. Wang, W. H. Jiang, W. Jiang and Z. X. Xie, Hydrothermal synthesis of highly fluorescent Ag-In-S/ZnS core/shell quantum dots for white light-emitting diodes, *J. Alloys Compd.*, 2019, **804**, 119–127.

52 H. T. Ma, L. J. Pan, J. Wang, L. Zhang and Z. L. Zhang, Synthesis of $AgInS_2$ QDs in droplet microreactors: Online fluorescence regulating through temperature control, *Chin. Chem. Lett.*, 2019, **30**(1), 79–82.

53 J. Y. Chang, G. Q. Wang, C. Y. Cheng, W. X. Lin and J. C. Hsu, Strategies for photoluminescence enhancement of $AgInS_2$ quantum dots and their application as bioimaging probes, *J. Mater. Chem.*, 2012, **22**, 10609–10618.

54 C. H. Lai, C. Y. Chiang, P. C. Lin, K. Y. Yang, C. C. Hua and T. C. Lee, Surface-Engineered Growth of $AgIn_5S_8$ Crystals, *ACS Appl. Mater. Interfaces*, 2013, **5**, 3530–3540.

55 L. H. Lin, C. C. Wu, C. H. Lai and T. C. Lee, Controlled Deposition of Silver Indium Sulfide Ternary Semiconductor Thin Films by Chemical Bath Deposition, *Chem. Mater.*, 2008, **20**, 4475–4483.

56 I. A. Mir, V. S. Radhakrishanan, K. Rawat, *et al.*, Bandgap Tunable AgInS based Quantum Dots for High Contrast Cell Imaging with Enhanced Photodynamic and Antifungal Applications, *Sci. Rep.*, 2018, **8**, 9322 (12 pages).

57 M. J. Rao, T. Shibata, S. Chattopadhyay and A. Nag, Origin of photoluminescence and XAFS study of $(ZnS)_{1-x}(AgInS_2)_x$ nanocrystals, *J. Phys. Chem. Lett.*, 2014, **5**, 167–173.

58 C. Zhang, Y. Dou, J. Chen, S. Fang, W. Xu, X. Wu, L. Hu, F. Liu, Y. Li and J. Li, Cubic-spinel $AgIn_5S_8$-based thermoelectric materials: synthesis, phonon transport and defect chemistry, *Mater. Today Energy*, 2022, **27**, 101029 (10 pages).

59 Y. Mi, A. Jiang, L. Kong, J. Wang, H. Guo and S. N. Luo, Amplified spontaneous emission and lasing from Zn-processed, $AgIn_5S_8$ core/shell quantum dots, *ACS Appl. Mater. Interfaces*, 2023, **15**, 19330–19336.

60 S. Jeong, M. Ko, S. Nam, J. H. Oh, S. M. Park, Y. R. Do and J. K. Song, Enhancement mechanism of quantum yield in core/shell/shell quantum dots of ZnS–$AgIn_5S_8$/$ZnIn_2S_4$/ZnS, *Nanoscale Adv.*, 2024, **6**, 925–933.

61 B. Cichy, D. Wawrzynczyk, M. Samoc and W. Stręk, Electronic properties and third-order optical nonlinearities in tetragonal chalcopyrite $AgInS_2$, $AgInS_2$/ZnS and cubic spinel $AgIn_5S_8$, $AgIn_5S_8$/ZnS quantum dots, *J. Mater. Chem. C*, 2017, **5**, 149–158.

62 X. Zheng, Y. Yang, Y. Song, Z. Ma, Q. Gao, Y. Liu, J. Li, X. Wu, X. Wang, W. Mao, W. Liu, Y. Shen and X. Tian, Recent advances in photocatalytic hydrogen evolution of $AgIn_5S_8$-based photocatalysts, *Interdiscip. Mater.*, 2023, **2**, 669–688.

63 O. Chen, *et al.*, Compact high-quality CdSe-CdS core-shell nanocrystals with narrow emission linewidths and suppressed blinking, *Nat. Mater.*, 2013, **12**, 445–451.

64 S. Xu, S. Kumar and T. Nann, Rapid synthesis of high-quality InP nanocrystals, *J. Am. Chem. Soc.*, 2006, **128**, 1054–1055.

65 C. H. Hwang, J. Park, M. Song, J. H. Lee and I. W. Shim, Syntheses of CdTe Quantum Dots and Nanoparticles through Simple Sonochemical Method under Multibubble Sonoluminescence Conditions, *Bull. Korean Chem. Soc.*, 2011, **32**(7), 2207–2211.

66 B. Pejova, E. Sherif and M. W. Minde, Sonochemically Synthesized Quantum Nanocrystals of Cubic $CuInS_2$: Evidence for Multifractal Surface Morphology, Size-Dependent Structure, and Particle Size Distribution, *J. Phys. Chem. C*, 2020, **124**(37), 20240–20255.

67 B. Pejova, I. Grozdanov, D. Nesheva and A. Petrova, Size-Dependent Properties of Sonochemically Synthesized Three-Dimensional Arrays of Close-Packed Semiconducting $AgBiS_2$ Quantum Dots, *Chem. Mater.*, 2008, **20**(7), 2551–2565.

68 B. Pejova, S. Premcheska and E. S. Miftar, From Self-Affine Ag to Mounded Ag@Ag_2O Core–Shell Nanoplasmonic Surfaces By Sonochemistry, *J. Phys. Chem. C*, 2023, **127**(23), 11204–11217.

69 V. Vighetto, A. Troia, M. Laurenti, M. Carofiglio, N. Marcucci, G. Canavese and V. Cauda, Insight into Sonoluminescence Augmented by ZnO-Functionalized Nanoparticles, *ACS Omega*, 2022, **7**, 6591–6600.

70 L. A. Crum, Resource Paper: Sonoluminescence, *J. Acoust. Soc. Am.*, 2015, **138**, 2181–2205.

71 G. Delgadoa, A. J. Moraa, C. Pinedab and T. Tinocob, Simultaneous Rietveld refinement of three phases in the Ag–In–S semiconducting system from X-ray powder diffraction, *Mater. Res. Bull.*, 2001, **36**, 2507–2517.

72 M. Eldesouki, Z. L. Abo-Shanab, M. El-Shafie, M. Abo-Riya and S. A. El-Kholy, Fabrication and evaluation of novel sulfur/epoxy resin composites, *Polym. Bull.*, 2023, **80**, 12047–12064.

73 A. G. Kalampounias, K. S. Andrikopoulos and S. N. Yannopoulosa, Probing the sulfur polymerization transition in situ with Raman spectroscopy, *J. Chem. Phys.*, 2003, **118**, 8460–8467.

74 K. S. Suslick and D. J. Flannigan, Inside a Collapsing Bubble: Sonoluminescence and the Conditions During Cavitation, *Annu. Rev. Phys. Chem.*, 2008, **59**, 659–683.

75 K. S. Suslick, Sonochemistry, *Science*, 1990, **247**, 1439–1445.

76 R. Pflieger, E. Fayard, C. Noel, S. Nikitenko and T. Belmonte, Molecular Emissions in Sonoluminescence Spectra of Water Sonicated under Ar-Based Gas Mixtures, *Ultrason. Sonochem.*, 2019, **58**, 104637.

77 C. A. Durante Rincón, L. T. Duran, J. E. Medina, J. A. Castro, M. Leon and J. R. Fermın, Structural and optical properties of $AgIn_5S_8$, *Int. J. Mod. Phys. B*, 2017, **31**, 1750246(10 pages).

78 N. M. Gasanly, A. Serpenguzel, A. Aydinli, O. Gurlu and I. Yilmaz, Donor-acceptor pair recombination in $AgIn_5S_8$ single crystals, *J. Appl. Phys.*, 1999, **85**, 3198–3201.

79 A. Usujima, S. Takeuchi, S. Endo and T. Irie, Optical and Electrical Properties of $CuIn_5S_8$ and $AgIn_5S_8$ Single Crystals, *Jpn. J. Appl. Phys.*, 1981, **20**, L505–L507.

80 C. Paorici, L. Zanotti, N. Romeo, G. Sberveglieri and L. Tarricone, Crystal growth and properties of the $AgIn_5S_8$ compound, *Mater. Res. Bull.*, 1977, **12**, 1207–1211.

81 M. Isik and N. Gasanly, Ellipsometry study of optical parameters of $AgIn_5S_8$ crystals, *Phys. B*, 2015, **478**, 127–130.

82 B. Cichy, D. Wawrzynczyk, M. Samocb and W. Strek, *J. Mater. Chem. C*, 2017, **5**, 149–158.

83 M. Grundmann, *The Physics of Semiconductors: An Introduction Including Nanophysics and Applications*, Springer International Publishing, Switzerland, 3rd edon, 2016.

84 B. Pejova, Optical absorption of semiconductor quantum dot solids, *Semicond. Sci. Technol.*, 2014, **29**, 045007 (15pp).

85 B. Pejova, The Urbach–Martienssen absorption tails in the optical spectra of semiconducting variable-sized zinc selenide and cadmium selenide quantum dots in thin film form, *Mater. Chem. Phys.*, 2010, **119**, 367–376.

86 G. Gong, Y. Liu, B. Mao, L. Tan, Y. Yang and W. Shi, Ag doping of Zn-In-S quantum dots for photocatalytic hydrogen evolution: Simultaneous bandgap narrowing and carrier lifetime elongation, *Appl. Catal., B*, 2017, **216**, 11–19.